crystals

MDPI

Article

Crystallographic Orientation of Grains Formed in the Laser Melt-Pool of $(CoCuFeZr)_{17}Sm_2$ Anisotropic Permanent Magnets

Felix Trauter *, Ralf Loeffler, Gerhard Schneider and Dagmar Goll *

Materials Research Institute, Aalen University, 73430 Aalen, Germany; ralf.loeffler@hs-aalen.de (R.L.); gerhard.schneider@hs-aalen.de (G.S.)

* Correspondence: felix.trauter@hs-aalen.de (F.T.); dagmar.goll@hs-aalen.de (D.G.); Tel.: +49-7361-576-1672 (F.T.); +49-7361-576-1601 (D.G.)

Abstract: Textured microstructures and anisotropic properties are key factors for the optimization of magnetic materials. Only for high texture grades can the remanence J_r and the maximum energy product $(BH)_{max}$ be maximized. In additive manufacturing such as laser powder bed fusion (PBF-LB), methods to achieve texture have to be developed. In this work, anisotropic $(CoCuFeZr)_{17}Sm_2$ sintered magnets have been used as a substrate in experiments featuring single laser tracks to study the relationships between crystallographic orientation of the substrate grains and crystallographic orientation of grain growth in the melt-pool. The <0001> crystal direction (*c*-axis) of the substrate has been systematically varied with respect to the orientation of the laser scan track on the specimen surface. Crystallographic orientations of the melt-pool and the substrate have been analyzed using electron backscatter diffraction (EBSD). It is found that if the *c*-axis is oriented perpendicular to the temperature gradient in the melt-pool, grains grow with orientation similar to that of the substrate grain. If the *c*-axis and the temperature gradient are oriented in the same direction, the grains grow with high misorientation to the substrate. The highest anisotropy in the melt-pool is achieved when the substrate's *c*-axis is oriented along the laser scan track. Under these conditions, 98.7% of the melt-pool area shows a misorientation <45° compared to the substrate orientation. The texture grade of the melt-pool area is comparable to that of the substrate magnet, at 91.8% and 92.2%, respectively.

Keywords: additive manufacturing; laser powder bed fusion (PBF-LB); tailored microstructure; permanent magnets; Sm-Co; Sm_2 $(CoCuFeZr)_{17}$; 2:17 magnet; textured solidification; EBSD

Citation: Trauter, F.; Loeffler, R.; Schneider, G.; Goll, D. Crystallographic Orientation of Grains Formed in the Laser Melt-Pool of $(CoCuFeZr)_{17}Sm_2$ Anisotropic Permanent Magnets. *Crystals* **2024**, *14*, 955. https://doi.org/10.3390/cryst14110955

Academic Editors: Erdem Karakulak and Marzena Lachowicz

Received: 1 October 2024
Revised: 27 October 2024
Accepted: 28 October 2024
Published: 31 October 2024

1. Introduction

Permanent magnets are important components in electric machines such as generators and motors and therefore are a key component in the transition to environmentally friendly energy generation and transportation. The most powerful FeNdB permanent magnets are manufactured by powder metallurgical processes, where a textured microstructure is realized by aligning powder particles in a magnetic field. The resulting magnets possess a high coercivity $\mu_0 H_c$, a high remanence J_r, and a high maximum energy product $(BH)_{max}$. The value of the remanence is highly dependent on the crystallographic orientation of the *c*-axis of individual grains (texture grade) that is achieved during processing [1,2]. Recently, alternative processing methods using additive manufacturing techniques have been tested. Using laser powder bed fusion (PBF-LB) additive manufacturing with FeNdB alloys has so far resulted in samples with nanocrystalline microstructures [3–7]. The samples showed high coercivities, however, with remanences around half of the saturation polarization J_s. This texture grade J_r/J_s~0.5 indicates a largely isotropic microstructure. Only in one case did PBF-LB processing of FeNdB result in a textured microstructure [8]. The samples showed a microstructure of fine lamellar $Fe_{14}Nd_2B$ phase with preferential growth along the building direction. This led to a crystallographic texture with *c*-axis orientation perpendicular to the building direction. However, due to the elongated grains and insufficient decoupling of grains by the grain boundary phase, the samples did not exhibit a high coercivity.

Using PBF-LB additive manufacturing for two other permanent magnetic materials, FePrCuB [9,10] and $(CoCuFeZr)_{17}Sm_2$ [11], samples with partial anisotropy could be produced. The two materials are known to show anisotropic microstructures when directional solidification occurs on the mold wall during casting [12–14] or when directional solidification techniques are used [15–19]. The cast samples do not exhibit high coercivity in the as-cast state. However, in both cases, high coercivities develop during subsequent heat treatment, during which the necessary phases and microstructures are formed. By PBF-LB additive manufacturing and subsequent material-specific heat treatment of Fe73.8-Pr20.5-Cu2.0-B3.7, Goll et al. [9] achieved a remanence of J_r = 0.67 T when measured with the magnetic field oriented along the scanning direction. With a saturation polarization of J_s = 1.0 T, this corresponds to a texture grade of J_r/J_s = 0.67. In the case of $(CoCuFeZr)_{17}Sm_2$ [11], PBF-LB manufactured and heat-treated samples resulted in a remanence of J_r = 0.78 T when measured with the magnetic field oriented along the scanning direction. Compared to an isotropic sintered magnet of similar composition and a remanence of J_r = 0.63 T, the remanence of the additively manufactured magnet is ~24% higher. With an estimated saturation polarization of J_s~1.2 T, the texture grade of the additively manufactured sample is J_r/J_s~0.65.

Assuming that the texture evolution in PBF-LB additive manufacturing could be understood, controlled, and maximized, the magnetic properties could be substantially improved. If a texture degree of J_r/J_s = 0.9 could be achieved, the resulting $(CoCuFeZr)_{17}Sm_2$ magnet would reach a remanence of up to J_r = 1.1 T and a maximum energy product of up to $(BH)_{max}$ = 220 kJ/m^3, respectively.

Recent work has shown how the laser parameters (laser power, scan velocity) and the resulting geometry of the melt-pool (depth, width) affect the solidification behavior of $(CoCuFeZr)_{17}Sm_2$ in the melt-pool [20]. Using single-track experiments on isotropic $(CoCuFeZr)_{17}Sm_2$ magnets, it was shown how an advantageous choice of parameters leads to columnar dendritic growth of grains. A preferred growth direction of the grains was found along the temperature gradient, perpendicular to the melt-pool boundary. In numerous of the analyzed melt-pools that exhibited columnar dendritic growth, the crystallographic orientation of some substrate grains was continued by the grains inside the melt-pool with little or no misorientation. In other areas of the same melt-pool, the orientation of the substrate was not continued, and the resulting crystallographic orientation of the corresponding grains inside the melt-pool differed strongly. This suggests that besides the temperature gradient, there is another factor influencing the growth of textured microstructures in the melt-pool. This additional influencing factor is assumed to be the crystallographic orientation of the substrate.

Research on textured microstructures in PBF-LB so far has been mainly focused on the influence of laser parameters and scanning strategies. Therefore, only little is known about the influence of textured substrates on the crystallographic orientation of grains formed in the melt-pool during the PBF-LB process. Few publications have analyzed the texture evolution for laser material deposition (LMD) of Ni-alloys on single crystal substrates [21–26]. It was found that the orientation of the substrate was continued in the deposited area with little misorientation when the substrate was oriented with the <001> crystal direction along the building direction. Only a small zone on the surface showed an equiaxed microstructure with isotropic orientation, caused by the faster cooling in contact with the atmosphere [21,26]. Furthermore, a relationship was found between the substrate orientation and the preferred growth direction in PBF-LB additive manufacturing of Ni- and Ti-alloys [27,28]. If the substrate was oriented with its preferred growth direction along the temperature gradient in the melt-pool, the crystallographic orientation was maintained during grain growth in the melt-pool [27]. If the substrate was oriented with the preferred crystal growth direction along the building direction, the crystallographic orientation of the substrate grains was continued in the built-up material with low misorientation. When the substrate orientation was changed to a different configuration, the resulting crystal growth direction increasingly deviated from the substrate orientation [27,28]. During laser

melting (e.g., in PBF-LB additive manufacturing), the temperature gradient is not uniform over the whole melt-pool area. According to experimental results and simulations from the literature [29–31], the temperature gradient is oriented approximately perpendicular to the melt-pool boundary and increases towards the bottom of the melt-pool. Therefore, the laser parameters (e.g., laser power P_L, scanning speed v_s) that determine the characteristics of the melt-pool (width, depth and aspect ratio) also influence the temperature gradient [31,32].

So far, all research in this field has been carried out on materials with cubic crystal structures, where the preferred crystal growth direction is <001>. This highly symmetric crystal structure makes the orientation of the substrate along the temperature gradient quite simple. $(CoCuFeZr)_{17}Sm_2$, on the other hand, features a complex crystal structure that varies with the annealing conditions. In the as-cast or as-built (in PBF-LB) condition, the microstructure comprises a hexagonal primary 17:2 phase (Th_2Ni_{17} type; a = 0.84 nm, c = 0.85 nm) and Sm-rich peritectic phase. During material-specific three-step heat treatment, a three-phase nanostructure is formed in a self-organized process [33,34]. It consists of Fe-rich rhombohedral 17:2 matrix phase (Th_2Zn_{17} type; a = 0.84 nm, c = 1.22 nm), hexagonal Cu-rich 5:1 ($CaCu_5$ type; a = 0.50 nm, c = 0.40 nm) cell walls and Zr-rich lamellae [35–38]. Both 17:2 crystal structures are based on the 5:1 type crystal structure and are formed by substitution of Sm atoms by Co and stacking of substituted layers [39]. Because of the similarity of these three phases, they can all be indexed in electron backscatter diffraction (EBSD) analysis using the Co_5Sm phase. It is known from the literature that the preferred crystal growth direction of the 17:2 phase can change from parallel to the <0001> direction to perpendicular to it in directionally solidified bulk samples, depending on the specific chemical composition and solidification conditions (temperature gradient and growth rate) [15,18,19]. In previous research on PBF-LB additive manufacturing of $(CoCuFeZr)_{17}Sm_2$, Goll et al. [11] found anisotropic microstructures with preferred growth along the building direction, with the <0001> crystal direction oriented perpendicular to that. The preferred crystal growth direction of $(CoCuFeZr)_{17}Sm_2$ in the scenario of solidification in the laser melt-pool is therefore assumed to be perpendicular to <0001>.

Single-track experiments have proven to be a useful strategy for efficient analysis of fundamental relationships of laser–material interaction (e.g., influence of laser power and scanning speed on melt-pool size and shape, on grain size and shape and solidification texture) in PBF-LB additive manufacturing of FeNdB- [6], $(CoCuFeZr)_{17}Sm_2$- [20], Al- [40,41], Cu- [42], Ni-alloys [42,43], steels [42] and alumina [44].

The objective of this work is to analyze the relationships between the crystallographic orientation of the substrate and the crystallographic orientations of the grains that have been formed in the laser melt-pool. Single-track laser experiments are performed on anisotropic $(CoCuFeZr)_{17}Sm_2$ sintered magnets. The orientation of the <0001> crystal direction in the substrate is systematically varied in respect to the laser scan vector. The resulting microstructure and texture in the melt-pools are analyzed using EBSD.

2. Materials and Methods

Single-track experiments were performed on anisotropic $(CoCuFeZr)_{17}Sm_2$ sintered magnets to investigate the relationship between the crystallographic orientation of the substrate grains and the crystallographic orientation of grains formed in the laser melt-pool efficiently. The sintered magnets of composition Co61.4-Cu6.2-Fe18.8-Zr1.9-Sm11.7 were provided by Arnold Magnetic Technologies. From the magnets, samples of size 20 mm × 20 mm × 3 mm (length l × width w × height h) were cut using a diamond band saw. The substrate magnets were ground by hand using 220 grit SiC-paper to achieve homogeneous absorption of the laser on the surface. The experiments were conducted under Ar atmosphere in a sealed processing chamber. A fiber laser (TruFiber 1000, TRUMPF, Ditzingen, Germany) with a wavelength of 1070 nm and a maximum output power of 1000 W was used to expose the samples. The exposed laser tracks had a length of 18 mm and a spacing of 1 mm between lines. For the experiments, the laser was defocused by 5 mm to increase the laser spot diameter from 46 µm (in focus) to 200 µm. Laser parameters

(laser power P_L = 200 W, scanning speed vs. = 800 mm/s), as well as the defocus, were derived from previous experiments [20]. In the previous experiments, these parameters produced a microstructure with mostly columnar dendritic growth in the melt-pool.

While the laser parameters are kept constant for all three samples, the orientation of the magnetically easy axis (*c*-axis, <0001> crystal direction) is systematically varied as shown in Figure 1. In the first sample (Figure 1a), the *c*-axis is oriented perpendicular to the laser scan vector and parallel to the direction of the laser beam, along the sample direction A1. In the second sample (Figure 1b), the *c*-axis is oriented perpendicular to the laser scan vector and the direction of the laser beam, along the sample direction A2. In the third sample (Figure 1c), the *c*-axis is oriented parallel to the laser scan vector, along the sample direction A3.

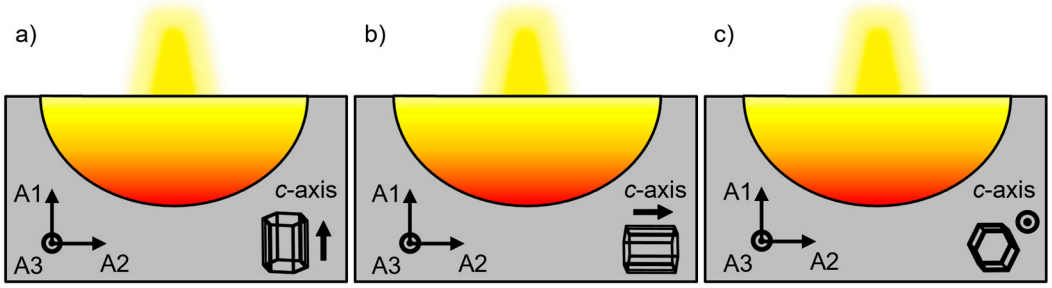

Figure 1. Schematic representation of the three different analyzed samples with their *c*-axis orientation in respect to the laser melt-pool. Each showing the sample coordinate system with the sample directions A1, A2 and A3, as well as the hexagonal $(CoCuFeZr)_{17}Sm_2$ unit cell with a black arrow indicating the *c*-axis orientation (<0001> crystal direction) in the substrate. The *c*-axis of the samples is oriented in (**a**) in vertical direction of the image plane, along sample direction A1, perpendicular to the laser scan track, (**b**) in horizontal direction of the image plane, along sample direction A2, perpendicular to the laser scan track, and (**c**) perpendicular to the image plane, along sample direction A3, parallel to the laser scan track.

To avoid damage during the following materialographic preparation, the samples were infiltrated with epoxy resin. Cross-sections of the samples were cut, using a high-precision diamond bandsaw. The cut samples were embedded in epoxy resin, and mechanically ground and polished. The polished microsections were analyzed in a scanning electron microscope (Sigma 300 VP, ZEISS, Jena, Germany) using EBSD with an EDAX camera and software (Hikari, OIM v8.6 orientation imaging microscopy, EDAX-Ametek, Weiterstadt, Germany).

From the EBSD scans, inverse pole figure maps, pole figures, crystal direction maps and crystal direction charts were created, to qualitatively and quantitatively analyze the textured microstructures of the substrate and the melt-pool of the three samples. The crystal direction maps and crystal direction charts were used to illustrate and quantify the orientation relationships between the microstructures in the substrate and the melt-pool. Additionally, a method to determine the direction of the temperature gradients in the melt-pool via analysis of the grain shape orientation angle from EBSD data from [20] was used. The reconstructed local temperature gradient was used to illustrate and discuss the relationships between the temperature gradient and the preferred crystal growth direction.

3. Results

The results of the three single-track experiments on anisotropic $(CoCuFeZr)_{17}Sm_2$ sintered magnets are presented in the following. In Figure 2, the inverse pole figure (IPF) maps (a–c) and corresponding pole figures (d–f) of the three single-track samples are illustrated. The melt-pool boundary is marked by a dashed line. The *c*-axis direction of the substrate is annotated in the IPF maps. The pole figures show points belonging to the melt-pool area in black and points from the substrate in blue. The three melt-pools show a depth of around 80–90 µm and a width of 160–175 µm. This accounts for a melt-pool aspect ratio of around 0.5. This value is higher than the aspect ratio of 0.3, achieved in previous

experiments with the same parameter set [20]. However, the microstructure of the three melt-pools shows mainly columnar dendritic growth, which was the main objective for the presented investigations.

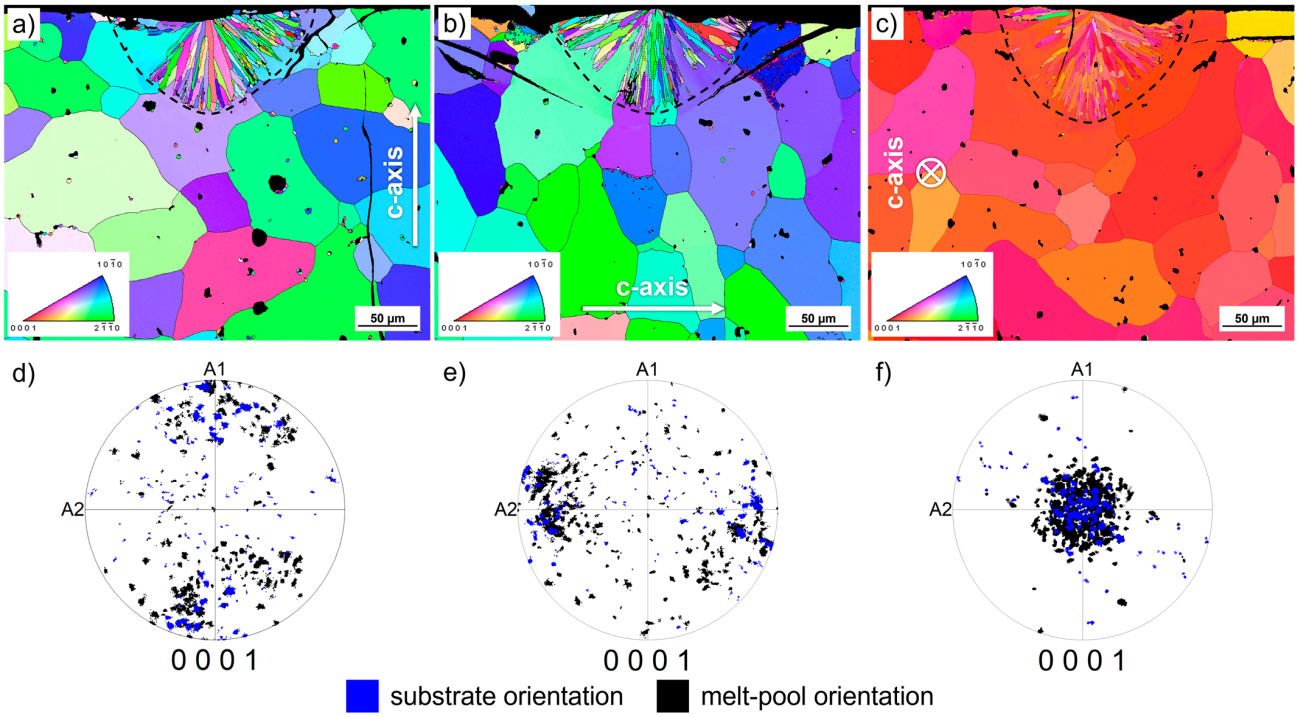

Figure 2. IPF maps (**a**–**c**) and corresponding pole figures (**d**–**f**) of three different melt-pools in anisotropic sintered magnets of $(CoCuFeZr)_{17}Sm_2$. The *c*-axis is oriented in (**a**,**d**) A1 direction, vertical direction of the image plane, perpendicular to the laser scan track; (**b**,**e**) A2 direction, horizontal direction of the image plane, perpendicular to the laser scan track; and (**c**,**f**) A3 direction, perpendicular to the image plane, parallel to the laser scan track. Color coding of the IPF maps shows the crystallographic orientation in respect to the sample direction A3 (out-of-plane). The melt-pool boundaries are marked by a dashed line. The *c*-axis direction of the substrate is noted in the images. The pole figures show points belonging to the substrate in blue and points belonging to the melt-pool in black.

In the first sample (Figure 2a,d), the *c*-axis is oriented in the vertical image direction, along the sample direction A1 (annotated in the pole figure). Except for one grain on the left side of the melt-pool, no clear relation between the orientation of grains in the substrate and melt-pool is visible in the IPF map. The pole figure shows a wider spread of the points from the melt-pool (black) than the substrate (blue), indicating a larger misorientation and thus lower anisotropy. The second sample (Figure 2b,e), with *c*-axis orientation in the horizontal image direction (along sample direction A2), shows a similar behavior. Only for one grain, a good correlation between the orientation of substrate and melt-pool grains is visible in the IPF map. Again, the pole figure shows a wider spread of points from the melt-pool (black) than from the substrate (blue), indicating a larger misorientation and thus smaller anisotropy. In the third sample (Figure 2c,f), the *c*-axis is oriented out-of-plane in the IPF map, along the sample direction A3. A good accordance of the orientation of the grains in the melt-pool and the substrate is visible, with most grains showing a red color, indicating an orientation of the <0001> crystal direction (*c*-axis) along the sample direction A3 (out-of-plane). The pole figure confirms this first impression, showing a similar spread of points from the melt-pool area (black) and the substrate (blue).

Although the IPF maps and pole figures represent a good overview of the crystallographic orientations in the acquired image area, it is difficult or impossible to deduce sufficient information about the anisotropy of the sample from those alone. One issue of

the IPF map is the missing information on orientation in the image plane. This becomes visible when comparing samples one (Figure 2a) and two (Figure 2b). Both show mainly blue and green grains, indicating an orientation of the crystal directions <10−10> and <2−1−10> along the sample direction A3, respectively. The different orientation of the *c*-axis, however, in both samples is not represented. The pole figure, on the other hand, shows this difference, but without spatial resolution.

These limitations require a different approach to visualize and quantify the orientation dependencies. In anisotropic permanent magnet materials, the orientation of the magnetically easy axis is of most interest. The sample direction in which the *c*-axis of most of the grains is oriented will exhibit the highest remanence and thus the highest $(BH)_{max}$ value. In $(CoCuFeZr)_{17}Sm_2$ magnets, this easy axis is the <0001> crystal direction (*c*-axis). To visualize the anisotropy, the misorientation of the <0001> crystal direction is shown for the three samples in Figure 3a,c. The reference direction for the misorientation is the sample direction in which the *c*-axis of the substrate magnet was oriented. For sample one, this is the sample direction A1, for the second sample, the sample direction A2, and for the third sample, the sample direction A3. The sample coordinate system is annotated in the images, and the corresponding reference direction is marked. To quantify these results, the angle between the <0001> direction and the reference sample direction for each pixel is plotted as cumulative number fractions in the graphs in Figure 3d–f. Each graph contains one dataset for the points that belong to the melt-pool and one for the points from the melt-pool. From the alignment angle graphs (Figure 3d–f), a mean misorientation can be calculated for the substrate and the melt-pool.

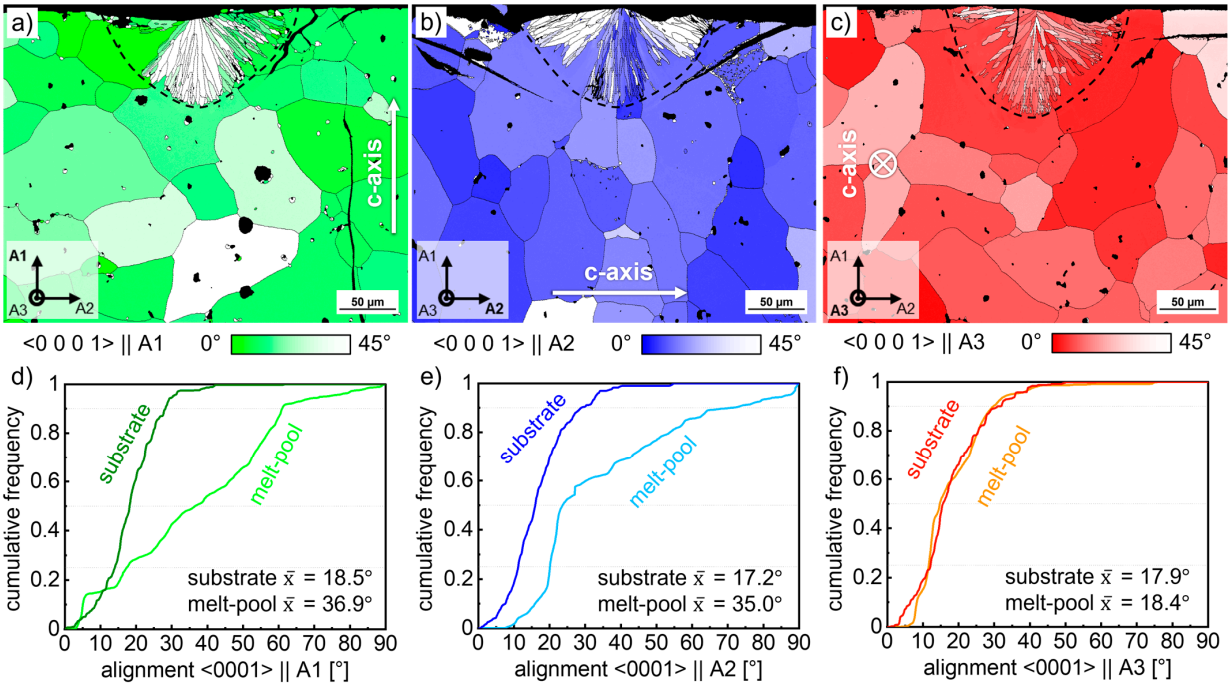

Figure 3. Crystal direction maps (top row) and corresponding crystal direction graphs of the three different samples shown in Figure 2. The angular deviation of the <0001> crystal direction of the grains from the (**a**,**d**) A1 sample direction, (**b**,**e**) A2 sample direction and (**c**,**f**) A3 sample direction is represented. The crystal direction maps (**a**–**c**) give a color-coded representation of the angular deviation from 0° to 45°. The melt-pool boundaries are marked by a dashed line. The crystal direction graphs (**d**–**f**) show the angular deviation of each point of the melt-pool and the substrate as cumulated curves. The mean misorientation angle for substrate and melt-pool is noted in each graph.

Figure 3a shows the alignment of the <0001> crystal direction along sample direction A1 in sample one. It shows a good alignment of the substrate grains around the melt-pool, as well as a good alignment of the grains on the left and right sides of the melt-pool. In

the center of the melt-pool, the grains show a misorientation of 45° or more. In general, only 55.8% of the melt-pool area shows a misorientation <45°. The alignment graph (Figure 3d) for sample one shows a strong deviation of the alignment in the melt-pool from the substrate. This is also reflected in the mean misorientation angle. The mean angle for the substrate is 18.5°, while the mean angle for the melt-pool is 36.9°. Figure 3b shows the alignment of the <0001> crystal direction along sample direction A2 in sample two. The grains on the sides of the melt-pool show a misalignment of 45° or more, while the grains in the center of the melt-pool show good alignment with the corresponding substrate grains. The alignment in the melt-pool of sample two seems more or less the inverse of the alignment in the melt-pool of sample one. In the melt-pool of sample two, 70.8% of the area shows a misorientation <45°. The alignment graph of sample two (Figure 3e) again reflects this partial alignment with higher misorientation in the melt-pool than in the substrate with mean misorientation angles of 35.0° and 17.2°, respectively. This difference in the mean misorientation angle of ~18° is similar to the difference in the mean angles of sample one. Figure 3c shows the alignment of the <0001> crystal direction along sample direction A3 in sample three. Sample three shows a quite good alignment of the grains in the whole melt-pool, with 98.7% of the melt-pool area showing a misorientation <45°. This is also reflected in the alignment graph (Figure 3f). The cumulative curves of the substrate and the melt-pool are congruent, and the mean alignment angles of the substrate and the melt-pool only differ by 0.5°, with 17.9° and 18.4°, respectively.

In sample three, the texture in the melt-pool was even high enough to calculate the degree of alignment from the EBSD analysis. In sample one and two, the texture is too weak for a quantitative analysis of the degree of alignment. While the substrate magnet shows a texturing degree of 92.2%, the texturing degree of the melt-pool area is insignificantly lower, at 91.8%.

4. Discussion

The results show that there are close relationships between the crystallographic orientation of the substrate and the microstructure and the crystallographic orientations in the melt-pool after solidification. According to the literature presented in Section 1—Introduction, it can be concluded that the preferred growth direction of the crystal lattice should be aligned in the same direction as the preferred growth direction of grains (along the temperature gradient) during solidification to achieve the best possible texture [27,28]. In the case of the laser melt-pool, the preferred grain growth direction is along the temperature gradient, which is always approximately perpendicular to the melt-pool boundary [29–31]. As established from the literature in Section 1—Introduction [11,15], the preferred crystal growth direction of $(CoCuFeZr)_{17}Sm_2$ in the laser melt-pool is perpendicular to the <0001> crystal direction. Figure 4 shows a schematic representation of the three samples from this work, with the temperature gradients in the melt-pool and the crystallographic orientation of the respective substrate material. For sample one (Figure 4a), the *c*-axis is perpendicular to the temperature gradient on the sides and parallel in the middle section of the melt-pool. Therefore, the preferred crystal growth direction and the temperature gradient are in parallel on the sides. This is reflected in the results presented in Figure 3a. The grains on the sides of the melt-pool adopt the favorable orientation of the substrate, while the grains in the middle section grow with large misorientation to the substrate grains.

For sample two (Figure 4b), this relation is inverted. The *c*-axis is in parallel to the temperature gradient on the sides and perpendicular in the middle; therefore, the preferred growth direction is in parallel to the temperature gradient in the middle section of the melt-pool. Again, this is reflected in the results for sample two, presented in Figure 3b, where the grains in the middle section of the melt-pool grow with the favorable crystallographic orientations of the substrate grains, while the grains on the sides of the melt-pool grow with different orientation to correct the unfavorable orientation of the substrate. In sample three (Figure 4c), the *c*-axis is oriented out-of-plane, while the temperature gradient is in-plane in the whole melt-pool. Therefore, the preferred growth direction of the crystal is in parallel

to the temperature gradient in the entire melt-pool area. This can be seen in the results in Figure 3c, where almost all grains in the melt-pool adopt the favorable crystallographic orientation of the substrate. These findings stand in good accordance with experimental results, as well as simulations from the literature [21,27,28,45]. Wherever the preferred grain growth direction along the temperature gradient and the preferred crystal growth direction from the substrate are parallel, the crystallographic orientation of the substrate grains is continued in the melt-pool.

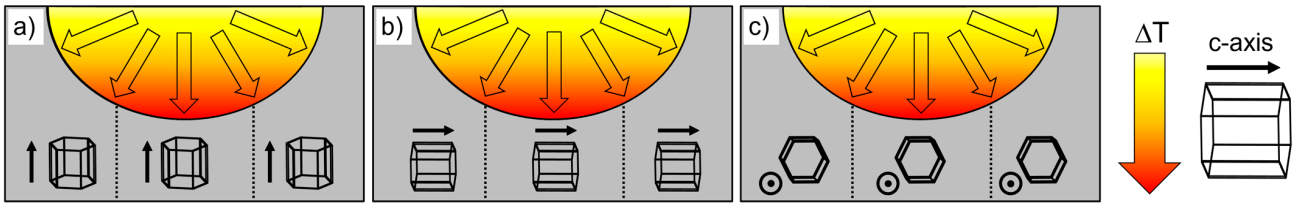

Figure 4. Schematic representation of the three different analyzed samples with the *c*-axis oriented (**a**) in vertical direction of the image plane, perpendicular to the laser scan track, (**b**) in horizontal direction of the image plane, perpendicular to the laser scan track, and (**c**) in perpendicular direction to the image plane, parallel to the laser scan track. Each showing the temperature gradient in the melt-pool as arrows with black outline, as well as the hexagonal $(CoCuFeZr)_{17}Sm_2$ unit cell with a black arrow indicating the *c*-axis orientation (<0001> crystal direction) in the substrate.

This schematic reduces the three-dimensional melt-pool into one plane perpendicular to the laser scan vector, and a secondary temperature gradient is found along the scan vector from the melt-pool to the already solidified material further back in the scan track. According to the literature [29–31,46,47], this gradient decreases from the front of the melt-pool to the back and can cause a slight angle in the grain growth towards the front on the scan track but does not significantly influence the growth direction of the columnar grains in the melt-pool [45,48]. Furthermore, the influence of the cooling rate is not taken deeper into consideration in the presented experiments. Like the temperature gradient, the cooling rate is not uniform throughout the melt-pool [29,30,49]. The cooling rate mainly affects the nucleation rate and thus the grain size. For the presented experiments, the grain size plays a negligible role, and the grain orientation should not be affected by the cooling rate.

To highlight the results of the experiments and to show the relations between the temperature gradient, the preferred growth direction, as well as the orientations of substrate and melt-pool grains, two substrate grains together with the grains growing from them in the melt-pool were extracted from the EBSD datasets: one where the preferred crystal growth direction of the substrate grain is in parallel to the temperature gradient, and one where it is perpendicular. Figure 5 shows the IPF-maps (Figure 5a,b) with the relevant grains (region of interest, ROI) highlighted. As a visual guide, the unit cell in its actual orientation is drawn inside the highlighted grains in some positions. The inset of Figure 5a,b shows the pole figure of the highlighted portion, with the substrate orientation marked in red, and the mean temperature gradient for the melt-pool grains as an arrow. The angle of the temperature gradient was determined by the method proposed in [20], by analyzing the grain shape orientation angle. Additionally, the crystal direction maps for the two extracted areas are shown in Figure 5c,d. The reference direction in each case is the crystal direction of the substrate grain with respect to A3. The legend IPF triangle shows the substrate orientation and the 10° tolerance.

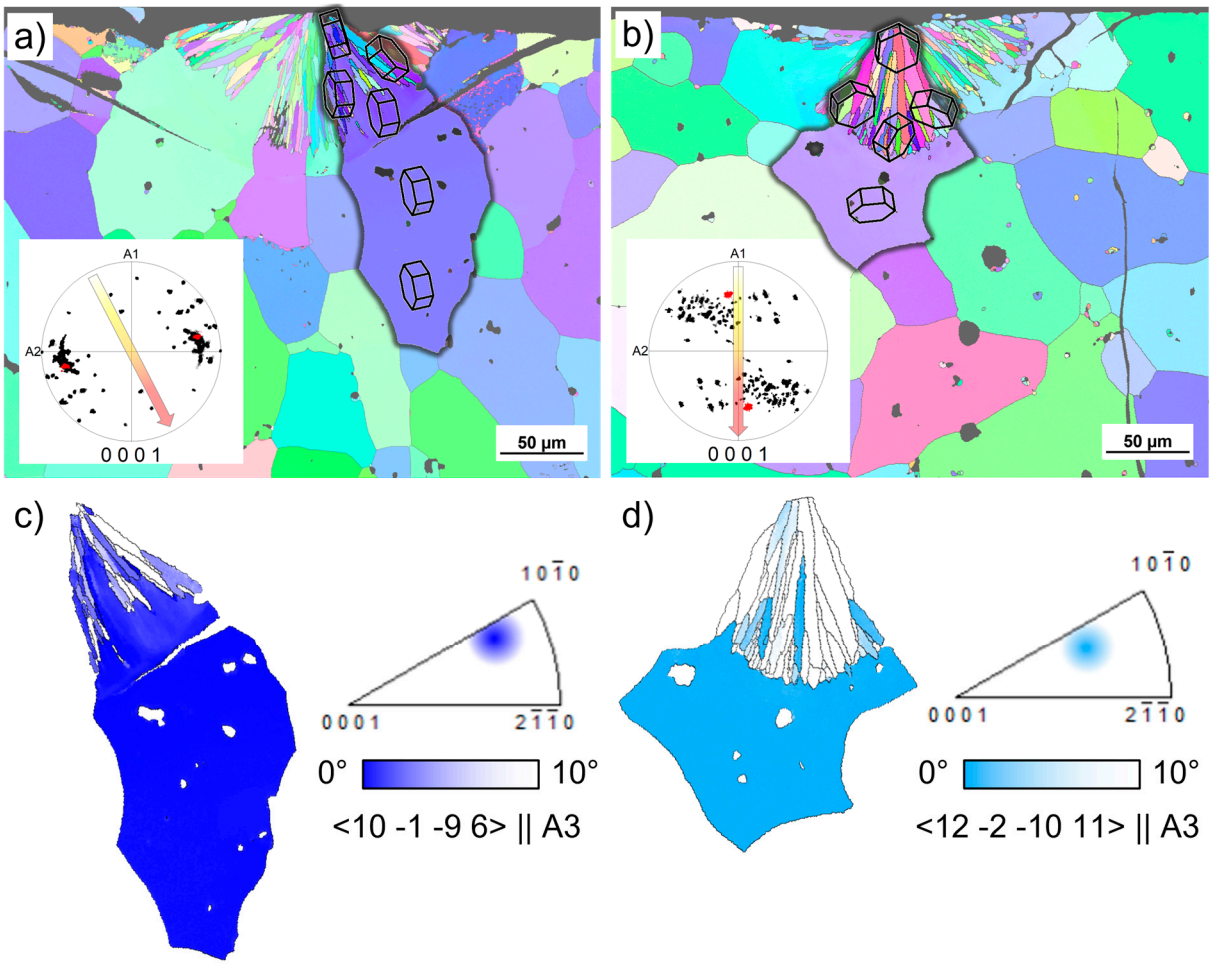

Figure 5. Exemplary representation of grains with (**a**,**c**) favorable and (**b**,**d**) unfavorable substrate orientation. (**a**,**b**) IPF-maps with highlighted region of interest (ROI) and unit cell drawings in the correct orientation are shown at several positions for visualization purposes. The inset shows the pole figure of the ROI with substrate orientation marked in red and an arrow indicating the mean temperature gradient in the melt-pool area of the ROI. (**c**,**d**) Crystal direction maps of the ROI with the substrate orientations (**c**) <10−1−9 6> and (**d**) <12−2−10 11> as reference direction. The IPF triangle with the respective reference crystal direction and 10° tolerance is shown as a legend.

From the pole figure in Figure 5a, the angle between the *c*-axis (<0001> crystal direction) of the substrate and the temperature gradient can be determined. Measured in clockwise direction from A1, the angle of the substrate grain *c*-axis is 77° as determined from the EBSD analysis. The mean angle of the temperature gradient in the ROI, calculated via the grain shape orientation, is 152°. Thus, the orientation of the preferred crystal growth direction, which is perpendicular to the grain *c*-axis (77° + 90° = 167°) corresponds very well to the orientation of the preferred grain growth along the temperature gradient (152°), having a difference of only 15°. The crystal direction map in Figure 5c shows the deviation of the grain orientation from the substrate orientation in the range from 0° to 10°. Eighty-four percent of the grain area belonging to the melt-pool shows a deviation <10°. Looking at the pole figure of the less favorable oriented grain in Figure 5b, the angle between the *c*-axis and the temperature gradient can be calculated. Here, the deviation of the temperature gradient from A1 is 182°, while the angle of the *c*-axis is 170°. This results in an angle of 78° between the preferred crystal growth direction and the preferred grain growth direction along the temperature gradient. The result of this large mismatch of the two angles can be seen in the crystal direction map in Figure 5d. Most of the area inside the melt-pool shows a deviation of > 10° from the substrate orientation, and only 28.2% of the melt-pool

grain area shows a deviation < 10°. As can be seen in the IPF-map and the pole figure in Figure 5b, the crystallographic orientation of the melt-pool grains is also spreading widely, resulting in a largely isotropic microstructure.

5. Conclusions

In this work, three single-track experiments on anisotropic sintered $(CoCuFeZr)_{17}Sm_2$-magnets were carried out to analyze the relationships between the crystallographic orientation of the substrate grains and the crystallographic orientation of grains that have been formed in the laser melt-pool. It was found that a strong relationship exists between the crystallographic orientation of the substrate grains and the crystallographic orientation of grains in the melt-pool after solidification. When the substrate provides an orientation where the preferred growth direction of the crystal structure is aligned in parallel to the preferred grain growth direction in the melt-pool along the temperature gradient, grains in the melt-pool grow with low misorientation (misorientation < 10°) from the substrate orientation.

For the $(CoCuFeZr)_{17}Sm_2$-alloy, the preferred crystal growth direction is perpendicular to the <0001> crystal direction (*c*-axis). Because the temperature gradient in the melt-pool is perpendicular to the melt-pool interface, its direction changes over the cross-section. Therefore, the use of anisotropic substrates with *c*-axis orientation perpendicular to the laser scan track, regardless of the laser beam direction (horizontal) or perpendicular to it (vertical), only parts of the melt-pool area show growth with low misorientation from the substrate. With these substrate orientations, only 55–70% of the melt-pool area showed misorientations of <45° to the substrate reference orientation, and the mean misorientation was around 18° higher than in the substrate. If the *c*-axis of the substrate is oriented along the scan track, the preferred crystal growth direction is parallel to the temperature gradient over the full cross-section of the melt-pool. Therefore, the entire melt-pool area shows a textured microstructure with low misorientation to the substrate orientation. Additionally, 98.7% of the melt-pool area shows misorientations <45°, and the mean misorientation angle is only 0.5° higher than in the substrate. For the sample with this *c*-axis orientation, the texture was good enough to calculate a texturing degree. With 91.8%, the texturing degree in the melt-pool is almost identical to the texturing degree of the substrate magnet with 92.2%. These insights are essential to further increase the maximum energy product $(BH)_{max}$ of PBF-LB additively manufactured $(CoCuFeZr)_{17}Sm_2$ permanent magnets.

Author Contributions: Conceptualization, D.G., F.T., R.L. and G.S.; methodology, D.G., F.T., R.L. and G.S.; software, F.T.; validation, D.G., F.T., R.L. and G.S.; formal analysis, F.T.; investigation, D.G., F.T., R.L. and G.S.; resources, D.G. and G.S.; data curation, D.G., F.T., R.L. and G.S.; writing—original draft preparation, D.G., F.T., R.L. and G.S.; writing—review and editing, D.G., F.T., R.L. and G.S.; visualization, F.T.; supervision, D.G. and G.S.; project administration, D.G.; funding acquisition, D.G. All authors have read and agreed to the published version of the manuscript.

Funding: This research was funded by the Deutsche Forschungsgemeinschaft (DFG, German Research Foundation) within the scope of the project Comet, project number 516736439. Publication funded by Aalen University of Applied Sciences.

Data Availability Statement: The original contributions presented in the study are included in the article; further inquiries can be directed to the corresponding authors.

Acknowledgments: The authors thank Gerhard Martinek, Dominic Hohs, Emanual Wengenmayr, Julian Schurr and Tim Schubert (all Aalen University) for assistance during preparation, processing, and analysis of the samples and for fruitful discussions. The authors thank Urs Wyss from Arnold Magnetic Technologies for providing Co–Sm anisotropic sintered magnets for the experiments performed.

Conflicts of Interest: The authors declare no conflicts of interest.

References

1. Herbst, J.F. R_2Fe_{14} B materials: Intrinsic properties and technological aspects. *Rev. Mod. Phys.* **1991**, *63*, 819–898. [CrossRef]
2. Kim, A.S.; Camp, F.E.; Stadelmaier, H.H. Relation of remanence and coercivity of Nd,(Dy)-Fe,(Co)-B sintered permanent magnets to crystallite orientation. *J. Appl. Phys.* **1994**, *76*, 6265–6267. [CrossRef]
3. Bittner, F.; Thielsch, J.; Drossel, W.-G. Laser powder bed fusion of Nd–Fe–B permanent magnets. *Prog. Addit. Manuf.* **2020**, *5*, 3–9. [CrossRef]
4. Bittner, F.; Thielsch, J.; Drossel, W.-G. Microstructure and magnetic properties of Nd-Fe-B permanent magnets produced by laser powder bed fusion. *Scr. Mater.* **2021**, *201*, 113921. [CrossRef]
5. Périgo, E.A.; Jacimovic, J.; García Ferré, F.; Scherf, L.M. Additive manufacturing of magnetic materials. *Addit. Manuf.* **2019**, *30*, 100870. [CrossRef]
6. Tosoni, O.; Borges Mendonça, E.; Reijonen, J.; Antikainen, A.; Schäfer, L.; Riegg, S.; Gutfleisch, O. High-coercivity copper-rich Nd-Fe-B magnets by powder bed fusion using laser beam method. *Addit. Manuf.* **2023**, *64*, 103426. [CrossRef]
7. Goll, D.; Trauter, F.; Bernthaler, T.; Schanz, J.; Riegel, H.; Schneider, G. Additive Manufacturing of Bulk Nanocrystalline FeNdB Based Permanent Magnets. *Micromachines* **2021**, *12*, 538. [CrossRef]
8. Goll, D.; Vogelgsang, D.; Pflanz, U.; Hohs, D.; Grubesa, T.; Schurr, J.; Bernthaler, T.; Kolb, D.; Riegel, H.; Schneider, G. Refining the Microstructure of Fe-Nd-B by Selective Laser Melting. *Phys. Status Solidi RRL* **2019**, *13*, 1800536. [CrossRef]
9. Goll, D.; Trauter, F.; Loeffler, R.; Gross, T.; Schneider, G. Additive Manufacturing of Textured FePrCuB Permanent Magnets. *Micromachines* **2021**, *12*, 1056. [CrossRef]
10. Schäfer, L.; Skokov, K.; Liu, J.; Maccari, F.; Braun, T.; Riegg, S.; Radulov, I.; Gassmann, J.; Merschroth, H.; Harbig, J.; et al. Design and Qualification of Pr–Fe–Cu–B Alloys for the Additive Manufacturing of Permanent Magnets. *Adv. Funct. Mater.* **2021**, *11*, 2102148. [CrossRef]
11. Goll, D.; Trauter, F.; Braun, P.; Laukart, J.; Loeffler, R.; Golla-Schindler, U.; Schneider, G. Additive Manufacturing of Permanent Magnets Based on $(CoCuFeZr)_{17}Sm_2$. *Phys. Status Solidi RRL* **2021**, *15*, 2100294. [CrossRef]
12. Kwon, H.W.; Bowen, P.; Harris, I.R. A study of Pr-Fe-B-Cu permanent magnetic alloys. *J. Alloys Compd.* **1992**, *182*, 233–242. [CrossRef]
13. Mycock, G.J.; Faria, R.; Harris, I.R. The microstructures and magnetic properties of some cast and annealed Pr-Fe-Cu-B alloys. *J. Alloys Compd.* **1993**, *201*, 23–28. [CrossRef]
14. Shimoda, T.; Akioka, K.; Kobayashi, O.; Yamagami, T.; Ohki, T.; Miyagawa, M.; Yuri, T. Hot-working behavior of cast Pr-Fe-B magnets. *IEEE Trans. Magn.* **1989**, *25*, 4099–4104. [CrossRef]
15. Plugaru, N.; Rubín, J.; Bartolomé, J. Structural and magnetic investigation of Co-rich Sm–Co unidirectionally solidified alloys. *J. Alloys Compd.* **2007**, *433*, 129–139. [CrossRef]
16. Zhang, T.; Liu, H.; Ma, Z.; Jiang, C. Single crystal growth and magnetic properties of 2:17-type SmCo magnets. *J. Alloys Compd.* **2015**, *637*, 253–256. [CrossRef]
17. Tang, W.; Zhang, Y.; Hadjipanayis, G.C. Directional solidification studies on Sm/sub 2/(Co,Cu,Fe,Zr)/sub 17/magnets. In Proceedings of the Digest of INTERMAG 2003. International Magnetics Conference (Cat. No.03CH37401), Digests of INTERMAG 2003, Boston, MA, USA, 28 March–3 April 2003; IEEE: New York, NY, USA, 2003; F06, ISBN 0-7803-7647-1.
18. Liu, X.; PAN, J.; Xu, Z.; Zhuang, J.; Liu, M.; Yu, D.; Shi, Z.; Fu, H. Machinable REPM with Excellent Intrinsic Coercive Force Prepared by DS Technology. *J. Mater. Sci. Technol.* **1997**, *13*, 475–478.
19. Liu, X.; Jing, P. Easy-Magnetization-Axis Arrangements of Sm_2Co_{17} and $RE_2Fe_{14}B$. *J. Rare Earths* **2006**, *24*, 302–305. [CrossRef]
20. Trauter, F.; Loeffler, R.; Schneider, G.; Goll, D. Shape Anisotropy of Grains Formed by Laser Melting of $(CoCuFeZr)_{17}Sm_2$. *Metals* **2024**, *14*, 1025. [CrossRef]
21. Gäumann, M.; Henry, S.; Cléton, F.; Wagnière, J.-D.; Kurz, W. Epitaxial laser metal forming: Analysis of microstructure formation. *Mater. Sci. Eng. A* **1999**, *271*, 232–241. [CrossRef]
22. Gäumann, M.; Bezençon, C.; Canalis, P.; Kurz, W. Single-crystal laser deposition of superalloys: Processing–microstructure maps. *Acta Mater.* **2001**, *49*, 1051–1062. [CrossRef]
23. Acharya, R.; Sharon, J.A.; Staroselsky, A. Prediction of microstructure in laser powder bed fusion process. *Acta Mater.* **2017**, *124*, 360–371. [CrossRef]
24. Acharya, R.; Bansal, R.; Gambone, J.J.; Kaplan, M.A.; Fuchs, G.E.; Rudawski, N.G.; Das, S. Additive Manufacturing and Characterization of René 80 Superalloy Processed Through Scanning Laser Epitaxy for Turbine Engine Hot-Section Component Repair. *Adv. Eng. Mater.* **2015**, *17*, 942–950. [CrossRef]
25. Basak, A.; Acharya, R.; Das, S. Epitaxial deposition of nickel-based superalloy René 142 through scanning laser epitaxy (SLE). *Addit. Manuf.* **2018**, *22*, 665–671. [CrossRef]
26. Acharya, R.; Bansal, R.; Gambone, J.J.; Das, S. A Coupled Thermal, Fluid Flow, and Solidification Model for the Processing of Single-Crystal Alloy CMSX-4 Through Scanning Laser Epitaxy for Turbine Engine Hot-Section Component Repair (Part I). *Met. Mater. Trans. B* **2014**, *45*, 2247–2261. [CrossRef]
27. Ishimoto, T.; Hagihara, K.; Hisamoto, K.; Nakano, T. Stability of crystallographic texture in laser powder bed fusion: Understanding the competition of crystal growth using a single crystalline seed. *Addit. Manuf.* **2021**, *43*, 102004. [CrossRef]
28. Yang, J.; Li, F.; Pan, A.; Yang, H.; Zhao, C.; Huang, W.; Wang, Z.; Zeng, X.; Zhang, X. Microstructure and grain growth direction of SRR99 single-crystal superalloy by selective laser melting. *J. Alloys Compd.* **2019**, *808*, 151740. [CrossRef]

29. Thijs, L.; Kempen, K.; Kruth, J.-P.; van Humbeeck, J. Fine-structured aluminium products with controllable texture by selective laser melting of pre-alloyed AlSi10Mg powder. *Acta Mater.* **2013**, *61*, 1809–1819. [CrossRef]
30. Krakhmalev, P.; Fredriksson, G.; Svensson, K.; Yadroitsev, I.; Yadroitsava, I.; Thuvander, M.; Peng, R. Microstructure, Solidification Texture, and Thermal Stability of 316 L Stainless Steel Manufactured by Laser Powder Bed Fusion. *Metals* **2018**, *8*, 643. [CrossRef]
31. Köhnen, P.; Létang, M.; Voshage, M.; Schleifenbaum, J.H.; Haase, C. Understanding the process-microstructure correlations for tailoring the mechanical properties of L-PBF produced austenitic advanced high strength steel. *Addit. Manuf.* **2019**, *30*, 100914. [CrossRef]
32. Attar, H.; Bönisch, M.; Calin, M.; Zhang, L.-C.; Scudino, S.; Eckert, J. Selective laser melting of in situ titanium–titanium boride composites: Processing, microstructure and mechanical properties. *Acta Mater.* **2014**, *76*, 13–22. [CrossRef]
33. Strnat, K. The hard-magnetic properties of rare earth-transition metal alloys. *IEEE Trans. Magn.* **1972**, *8*, 511–516. [CrossRef]
34. Livingston, J.D.; Martin, D.L. Microstructure of aged $(Co,Cu,Fe)_7Sm$ magnets. *J. Appl. Phys.* **1977**, *48*, 1350–1354. [CrossRef]
35. Fidler, J.; Skalicky, P. Microstructure of precipitation hardened cobalt rare earth permanent magnets. *J. Magn. Magn. Mater.* **1982**, *27*, 127–134. [CrossRef]
36. Kronmuller, H.; Durst, K.-D.; Ervens, W.; Fernengel, W. Micromagnetic analysis of precipitation hardened permanent magnets. *IEEE Trans. Magn.* **1984**, *20*, 1569–1571. [CrossRef]
37. Hadjipanayis, G.C.; Tang, W.; Zhang, Y.; Chui, S.T.; Liu, J.F.; Chen, C.; Kronmuller, H. High temperature 2:17 magnets: Relationship of magnetic properties to microstructure and processing. *IEEE Trans. Magn.* **2000**, *36*, 3382–3387. [CrossRef]
38. Goll, D.; Kronmüller, H.; Stadelmaier, H.H. Micromagnetism and the microstructure of high-temperature permanent magnets. *J. Appl. Phys.* **2004**, *96*, 6534–6545. [CrossRef]
39. Stadelmaier, H.H.; Reinisch, B.; Petzow, G. Samarium-Cobalt Phase Equilibria Revisited; Relevance to Permanent Magnets. *Int. J. Mater. Res.* **1998**, *89*, 114–118. [CrossRef]
40. Aboulkhair, N.T.; Maskery, I.; Tuck, C.; Ashcroft, I.; Everitt, N.M. On the formation of AlSi10Mg single tracks and layers in selective laser melting: Microstructure and nano-mechanical properties. *J. Mater. Process. Technol.* **2016**, *230*, 88–98. [CrossRef]
41. Aversa, A.; Moshiri, M.; Librera, E.; Hadi, M.; Marchese, G.; Manfredi, D.; Lorusso, M.; Calignano, F.; Biamino, S.; Lombardi, M.; et al. Single scan track analyses on aluminium based powders. *J. Mater. Process.* **2018**, *255*, 17–25. [CrossRef]
42. Yadroitsev, I.; Gusarov, A.; Yadroitsava, I.; Smurov, I. Single track formation in selective laser melting of metal powders. *J. Mater. Process. Technol.* **2010**, *210*, 1624–1631. [CrossRef]
43. Ghosh, S.; Ma, L.; Levine, L.E.; Ricker, R.E.; Stoudt, M.R.; Heigel, J.C.; Guyer, J.E. Single-Track Melt-Pool Measurements and Microstructures in Inconel 625. *JOM* **2018**, *70*, 1011–1016. [CrossRef]
44. Fan, Z.; Lu, M.; Huang, H. Selective laser melting of alumina: A single track study. *Ceram. Int.* **2018**, *44*, 9484–9493. [CrossRef]
45. Liu, J.; To, A.C. Quantitative texture prediction of epitaxial columnar grains in additive manufacturing using selective laser melting. *Addit. Manuf.* **2017**, *16*, 58–64. [CrossRef]
46. Kreitcberg, A.; Brailovski, V.; Sheremetyev, V.; Prokoshkin, S. Effect of Laser Powder Bed Fusion Parameters on the Microstructure and Texture Development in Superelastic Ti–18Zr–14Nb Alloy. *Shap. Mem. Superelasticity* **2017**, *3*, 361–372. [CrossRef]
47. Ehsan Saghaian, S.; Nematollahi, M.; Toker, G.; Hinojos, A.; Shayesteh Moghaddam, N.; Saedi, S.; Lu, C.Y.; Javad Mahtabi, M.; Mills, M.J.; Elahinia, M.; et al. Effect of hatch spacing and laser power on microstructure, texture, and thermomechanical properties of laser powder bed fusion (L-PBF) additively manufactured NiTi. *Opt. Laser Technol.* **2022**, *149*, 107680. [CrossRef]
48. Wang, Y.; Shi, J.; Liu, Y. Competitive grain growth and dendrite morphology evolution in selective laser melting of Inconel 718 superalloy. *J. Cryst. Growth* **2019**, *521*, 15–29. [CrossRef]
49. Hasanabadi, M.; Imani Shahabad, S.; Keshavarzkermani, A.; Eybel, R.; Gerlich, A.; Toyserkani, E. A numerical modelling for laser powder-bed fusion of Ti-alloy with a hybrid heat source: An investigation on solidification and microstructure formation. *Opt. Laser Technol.* **2024**, *174*, 110647. [CrossRef]